RSC
Applied Interfaces

ROYAL SOCIETY
OF CHEMISTRY

PAPER

View Article Online
View Journal | View Issue

Check for updates

Cite this: *RSC Appl. Interfaces*, 2025, **2**, 1877

Tin-oxide-based binder-free lightweight nanostructured anode with high reversible capacity and cyclability for lithium-ion batteries, manifesting the interfacial effect

Adi Pratap Singh,† Banadeep Dutta† and Sudeshna Chattopadhyay *

Received 2nd September 2025,
Accepted 30th September 2025

DOI: 10.1039/d5lf00261c

rsc.li/RSCApplInter

Advancements in lithium-ion batteries (LIBs) that deliver higher storage capacity, energy density, and power density are essential to meet the growing power demands of modern technologies. The increasing use of lightweight micro-devices in flexible and portable electronics—such as wearable health monitors, implanted medical devices, smart cards, and IoT sensors—further emphasizes the need for miniaturization of energy storage. This report describes a high-performance, lightweight, binder-free tin-oxide (SnO_2)-based nanostructured thin-film anode on a copper (Cu) current collector for rechargeable LIBs, with lithium foil as the counter electrode. Importantly, the fabrication process of this binder-free electrode does not involve any binder, conductive agent or other additional inactive components (unlike the typical electrode preparation method), which results in improved energy density by reducing the effective weight of the LIB. Furthermore, it eliminates weak interaction and interface issues between binder and electrode material, thus minimizing the possibility of self-aggregation of active materials, besides providing increased accessibility of the electrolyte to the active material. The fabricated half-cell exhibits significantly high reversible capacities of 1430 mAh g^{-1} and about 1200 mAh g^{-1} after 100 and 500 cycles, respectively, at a current density of 0.3 A g^{-1} (0.2C), excellent cyclability, rate performance (~800 mAh g^{-1} at 3 A g^{-1} at 110 cycles) and stability with a high Coulombic efficiency (98–99%), as tested in the 0.02 to 1.8 V window. Activation of the electrode was achieved by a controlled post-deposition annealing process of optimized SnO_2 film on Cu, providing a suitable nanostructured hierarchical morphology and conformation involving an SnO_2–Cu interface, which facilitates good electrical contact and enhanced electron/ion transport kinetics, yielding high cyclability, rate performance and stability, preventing pulverization. Moreover, it introduces an extra interfacial charge storage phenomenon *via* Cu/Li_2O nanocomposites, resembling capacitive characteristics. Stable capacity involving SnO_2 dealloying–alloying along with the interface induced extra lithium storage capability, which contributed to accomplishing the observed high specific capacity of the electrode. This study provides an insight into the design of an advanced lightweight electrode for next-generation energy storage devices.

Introduction

As the global push for sustainable energy accelerates, the demand for efficient, scalable, and reliable energy storage systems (ESS) has surged. Driven by the rapid growth of renewable energy sources, such as solar and wind, which are inherently intermittent, energy storage has become a critical component in ensuring a stable and resilient power supply.[1] Furthermore, the need for creative storage solutions to satisfy a variety of applications has increased due to developments in distributed energy systems, smart grids, and electric vehicles (EVs).[1,2] Batteries, being a class of energy storage, in general, play a crucial role in ensuring on-demand energy supply, with equal importance to energy production. Modern requirements emphasize the development of energy storage systems that are lightweight, flexible, environmentally friendly, and cost-effective with enhanced performance. Lithium-ion batteries (LIBs) have the highest energy density per unit volume or mass[3] and have been utilized to power a wide variety of electronic devices.[3,4] Intercalation-based lithium-ion batteries operate by inserting and extracting Li^+ ions into and from anode and cathode materials.[5] To obtain high energy density and a longer cycling life, it is critical to

---

Department of Physics, Indian Institute of Technology Indore, Indore 453552, India. E-mail: sudeshna@iiti.ac.in, chattopadhyay.sudeshna@gmail.com

† Equal contribution and co-first authors.

improve the reversibility of Li^+ insertion and extraction.[5] The production of lithium oxide (Li_2O) is a significant issue in oxide-based lithium-ion batteries. The formation of Li_2O results in high capacity, but Li^+ extraction from Li_2O is irreversible, as observed for oxide-based electrodes, resulting in limited reversibility in rechargeable Li-ion batteries.[6] When it comes to energy density, the working voltage (V) and specific capacity (mAh g^{-1}) of the electrodes, along with an appropriate operating potential window, are its primary determinants.[7] Moreover, in typical electrode fabrication, a pasted electrode is created on the current collector by combining active materials with a conductive additive and binder.[8] The presence of binders and other inactive components leads to weak interactions and the interfacial problems between binder and electrode materials. This often causes self-aggregation of active materials, ultimately diminishing the overall battery performance. The use of binder-free electrodes not only minimizes these issues but also shows high electrolyte wettability.[9] Furthermore, binder-free thin-film batteries offer the advantage of direct growth of active materials on the current collector, thereby reducing the overall weight of the active electrode material and hence, increasing the energy density of the active electrode,[9] offering distinct advantages, including long cycle life, and the ability to operate safely over a wide range of temperatures.[10] Additionally, their compatibility with flexible substrates and ease of integration into microdevices[11] make them ideal for next-generation applications. Sectors such as healthcare, where thin-film battery-powered advanced wearable biosensors and implantable medical devices, and electronics, where they enable slimmer and smarter gadgets, are driving demand for these cutting-edge solutions.[12] Despite these advantages, the fabrication of binder-free electrodes faces several challenges. One key aspect is ensuring the compatibility between the electrode and current collector materials to achieve proper adhesion (*i.e.*, the adhesion energy between the materials should be greater than the cohesion energy of the deposited electrode material), thereby enabling the formation of a stable, wetting thin-film electrode.[13] The adhesion between two materials may depend on their relative surface energy; alternatively, it may rely on their relative dielectric polarizabilities.[13] Thus, to grow an efficient binder-free thin-film battery, where the active electrode material grows directly on a current collector, it is crucial to ensure excellent adhesion capability of the electrode material on the current collector, and, hence, good electrical conductivity at the electrode–current collector interface. Mechanical interlocking of the deposited material induced by substrate material/roughness also promotes adhering ability.[14,15] Furthermore, a particular deposition technique, such as magnetron sputter deposition,[16] plays a role in this respect by yielding a favourable interface (even a chemically rich one), and hence, better adhesion.[16,17] Additionally, the drive for eco-friendly and sustainable green technology emphasizes the significance of binder-free thin-film batteries, employing safer materials, for superior recyclability, with reduced environmental impact.

Therefore, numerous efforts have been made to investigate novel high-capacity electrode materials to replace standard graphite electrodes, which have a de-lithiation potential of approximately 0.3 V (*vs.* Li/Li^+)[18] and a low theoretical specific capacity of 372 mAh g^{-1}. Several materials have been studied as high-capacity anodes over the last two decades, including alloying-type metals like Sn, Al, Si, and Ge that can deliver capacities greater than 1000 mAh g^{-1} at potentials of ∼0.5 V, and conversion-type transition metal oxides (MOx) like Co_3O_4, Fe_2O_3, and CuO that have capacities of ∼800 mAh g^{-1} when de-lithiated at potentials over 2.0 V.[19] Among these, tin oxide (SnO_2) has garnered a lot of interest because of its high gravimetric capacity at moderate operating potential.[20] The electrochemical lithiation of SnO_2 involves a conversion process ($SnO_2 + Li^+ \rightarrow Sn + Li_2O$) with a potential plateau of about 1.2 V and an alloying reaction ($Sn + xLi^+ \rightarrow Li_xSn$) at about 0.5 V.[21] These reactions correspond to specific capacities of 711 and 783 mAh g^{-1}, respectively.[22] However, the following problems mostly prevent SnO_2 from reaching its full potential: (i) the occurrence of substantial volume changes during the intercalation and de-intercalation of Li^+ ions, causing issues of pulverization and detachment of active electrode material from the current collector, resulting in significant capacity degradation;[23] (ii) the low conductivity of SnO_2 at room temperature leads to a reduced electron transfer rate and sluggish reaction kinetics;[24] and (iii) Sn coarsening is another critical factor impacting capacity retention and contributing to the poor electrochemical performance of SnO_2.[25] This process promotes the agglomeration and growth of Li_2O particles or clusters, reducing electrical conductivity and hindering electron transfer to the inner Sn particles. As a result, the reversibility of the alloying and dealloying reactions in Sn particles deteriorates.[25,26]

To overcome these issues, different approaches involving the implementation of varieties of nanostructured SnO_2 systems[22,25,27] along with the introduction of suitable interfaces[28] have been reported in the literature.[22,25,27–29]

Nanostructured systems, in general, offer i) shorter Li^+ diffusion paths, leading to faster reaction kinetics; ii) better accommodation of volume expansion; iii) a larger surface area, providing more active sites for electrochemical reactions; and iv) improved electronic pathways, thereby overcoming the low conductivity issues,[30] particularly in metal oxides, and play a huge role in enhancing battery performance.[30,31] For SnO_2, the low conversion reaction reversibility and the pulverization problem are the primary factors responsible for the degradation in the performance of the battery. However, nanostructured SnO_2 has the potential to partially overcome the reversibility issues of the conversion reaction due to enhanced inter-diffusion kinetics at the Sn/Li_2O interface, resulting from the shorter transfer distances of Li^+ and electrons.[3,22,25] Conversely, nanocrystalline SnO_2 helps in effectively reducing the volume stress induced, thus overcoming the pulverization problem.[29,32] Subsequently, interface designing of SnO_2 nanostructured systems has also received attention, as this engineered interface facilitates smooth lithiation/de-lithiation processes with faster Li^+ diffusion kinetics and hinders the Sn coarsening problem, which results in an enhancement in lithium storage reaction reversibility.[28] In addition, the excellent inherent adhesion capability of SnO_2 on a conventional current collector (such as copper)[13,33] enhances its potential as a binder-free electrode material.

In this article, we report the development of a high-performance binder-free tin-oxide (SnO_2)-based thin-film electrode with a copper (Cu) current collector, introducing structural advantages at the Cu–SnO_2 interface, through a controlled post-deposition heat-treatment process. The thin Cu sheet acts as a current collector and substrate for SnO_2 sputter deposition. The SnO_2-based electrode exhibits high specific capacity with stable capacity retention, for half-cell tests with a lithium (Li) sheet as counter electrode, in applications for rechargeable thin-film Li-ion batteries (LIBs). We demonstrate that the post-deposition heat treatment induces a designed hierarchical structure in an electrode involving SnO_2 thin film on Cu. This process creates a suitable interface, which significantly enhances the effective conductivity of the system, and improves charge transfer properties. Additionally, it suppresses the pulverization problem in the SnO_2 active materials and activates extra interfacial charge storage capacity. As a result, the electrode exhibits an overall enhanced energy density, improved rate performance, better stability and longer cycle life, making it a high-performance candidate for rechargeable micro-battery systems.

Result and discussion

In this work, a new class of binder-free tin-oxide (SnO_2)-based thin-film electrode with a copper (Cu) current collector was investigated. Fig. 1(a) shows the X-ray photoelectron spectroscopy (XPS) studies of the sputter deposited (RF) thin film (as detailed in the experimental section), signifying the formation of SnO_2, while Fig. 1(b) provides the tentative thickness of the deposited film, which was found to be about 60 nm, from cross-sectional field emission scanning electron microscopy (FESEM) images. Fig. 1a(i–iii) shows the XPS spectra of core Sn 3d and O 1s for the sputter deposited sample. Strong signals of Sn $3d_{5/2}$ and Sn $3d_{3/2}$ were present at 486.5 eV (Fig. 1a(i)) and 495 eV (Fig. 1a(ii)), respectively, whereas there was a strong O 1s signal at 530.3 eV (Fig. 1a(iii)), convincingly corresponding to the formation of SnO_2.[34] No signals corresponding to the underlying Cu current collector were observed in the XPS spectra, indicating high coverage of pristine SnO_2 thin film. Overall, the XPS and cross-sectional FESEM results in Fig. 1 signify the deposition of a pristine SnO_2 thin film of about 60 nm of thickness on the Cu current collector *via* RF-sputtering. Further XPS study of the system after employing a controlled post-deposition heat-treatment process, is discussed later in the manuscript in the context of an electrochemical performance study of the electrode of interest, towards the

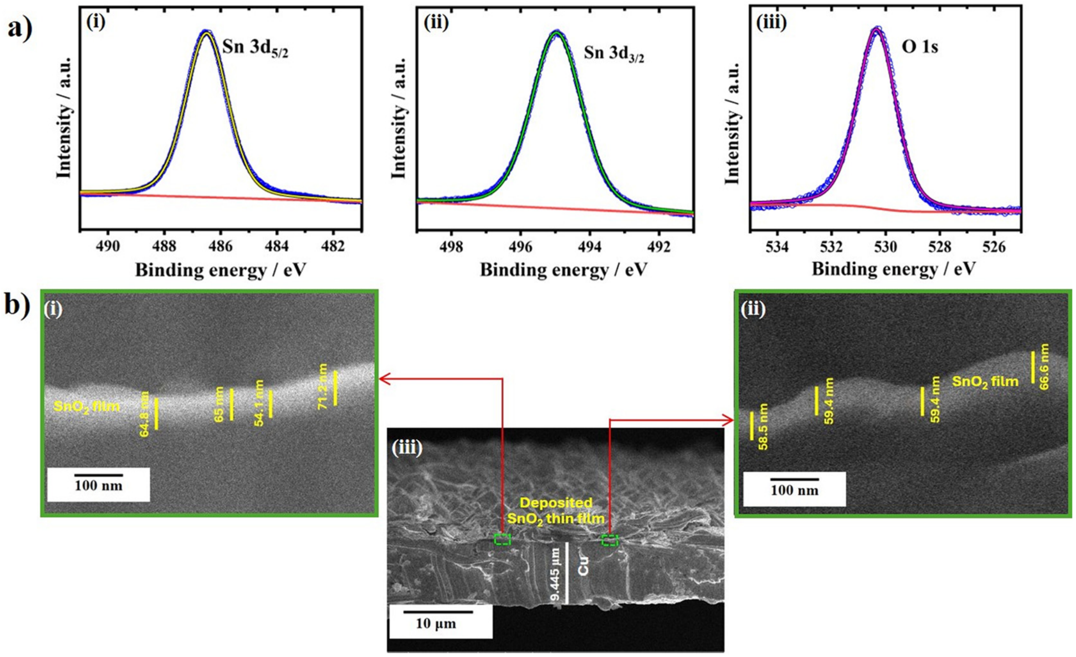

Fig. 1 Pristine SnO_2 thin film (RF-magnetron sputter deposited) on Cu current collector. (a) XPS spectra of Sn $3d_{5/2}$ (i), Sn $3d_{3/2}$ (ii) and O 1s (iii), signifying the deposited SnO_2 film. (b) Cross-sectional FESEM images at two different magnifications with respective scale bars; two magnified images (i)–(ii), indicating thickness of the deposited SnO_2 thin film, along with the overall cross-sectional image of the RF sputter deposited SnO_2 thin film on Cu current collector (iii).

explanation of the mechanism, and incorporated accordingly in SI, Fig. S1.

Electrochemical studies

Galvanostatic discharge–charge (GCD). The electrochemical performance of the LIB, comprising an SnO_2-based binder-free thin-film electrode (of about 60 nm thickness) with a Cu current collector, and Li as counter electrode or anode, has been explored. Controlled heat treatment of magnetron sputter deposited SnO_2 thin film on the Cu current collector forges the electrode of interest here (called the A-SnO_2 electrode) for application as a rechargeable Li-ion battery (LIB), as demonstrated in Fig. 2. Fig. 2(a) shows the galvanostatic discharge–charge (GCD) profiles of the battery, cycled between 0.02 V and 1.8 V, at a current density of 0.3 A g^{-1} for different cycles. The specific voltage window (0.02 V to 1.8 V) has been selected to probe the specific capacity corresponding to the SnO_2 system, involving an alloying/dealloying reaction at about 0.5 V. Cycle performance and Coulombic efficiency plots at the same current density of 0.3 A g^{-1} are shown in Fig. 2(b). The system provides extremely high capacity in the initial 15 cycles, of more than 2000 mAh g^{-1}, with sharp capacity fading with increasing cycle numbers, indicating irreversible reactions or the formation of a solid–electrolyte interphase (SEI), which occurred in this voltage window. It starts to become stable from 35 cycles onwards, *i.e.*, 1700 mAh g^{-1} at 35 cycles, reaching 1430 mAh g^{-1} at 110 cycles, and maintaining a reasonably stable value thereafter. Specific capacity remains steady at around 1200 mAh g^{-1} from 250 cycles to 500 cycles, and onwards. This result implies that the post-deposited heat-treated SnO_2 thin film on the Cu current collector delivers higher specific capacity in comparison to that of the experimental results reported in the literature involving various SnO_2-based electrodes (which was found to have a maximum value of about 800 mAh g^{-1}).[3,22,25,27,29] Secondly, the observed stable capacity, 1200 mAh g^{-1} (at higher cycle number, >250 cycles) is greater than the theoretical capacity of the alloying/dealloying reaction alone (*i.e.*, 783 mAh g^{-1}), signifying the activation of some other reactions or influences based on the interfacial effects in the SnO_2 nanostructured electrode system, which will be discussed and explained in the following section, in connection with the cyclic voltametric (CV) response of the system. A high Coulombic efficiency (~98–99%) is evident for this system (Fig. 2(b)). Furthermore, the

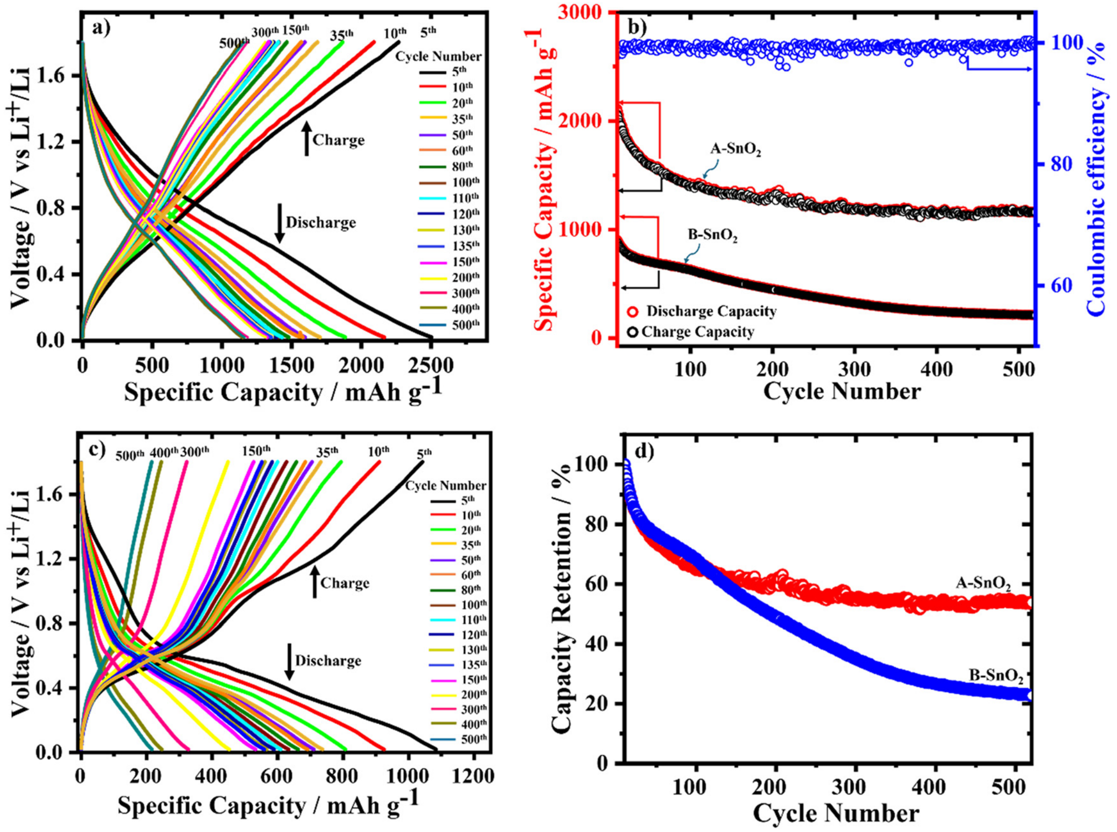

Fig. 2 Electrochemical characterization of electrodes A-SnO_2 and B-SnO_2. (a) Galvanostatic charge–discharge profiles of the A-SnO_2 electrode at a current density of 0.3 A g^{-1} for different cycles. (b) Cycle performances (from 10th to 520th cycle) of both electrodes along with the Coulombic efficiency plot of A-SnO_2 electrode, at a current density of 0.3 A g^{-1}. (c) Galvanostatic charge–discharge profiles of the B-SnO_2 electrode at a current density of 0.3 A g^{-1} for different cycles. (d) Capacity retention (from 10th to 520th cycle) of A-SnO_2 and B-SnO_2 electrodes.

electrode exhibits remarkably high stability and long cycle life (Fig. 2(a), (b), and (d)), compared to other available/reported SnO_2-based electrodes,[3,22,25,27,29,35] and hence reveals the remarkably high performance of the system. The observed electrochemical performance of A-SnO_2 is also superior to that of other available/reported thin-film electrodes, including other tin-oxide-based electrodes,[3,22,35,36] when used in equivalent micro-battery systems.[3,22,25,27,35–37] Relevant comprehensive information is shown in Table S1.

A comparison study using an equivalent untreated SnO_2 thin-film electrode on a Cu current collector was carried out, as presented in Fig. 1(b–d). Growth parameters for RF-sputter deposited SnO_2 were kept the same for both electrode systems (as discussed in the experimental section). Optimization of the growth parameters was carried out to obtain a high-quality film to achieve better performance of the electrode.

For convenience, from now on in this report, SnO_2 thin film on Cu current collector systems before and after post-deposition heat-treatment are referred as the untreated SnO_2 electrode ("B-SnO_2") and the electrode of interest ("A-SnO_2"), respectively.

Both treated and untreated SnO_2 electrodes (A-SnO_2 and B-SnO_2) exhibit an initial high capacity with a sharply falling trend over the first few cycles, as shown in Fig. 2(b) and (d), which can be attributed to the irreversible reactions or solid–electrolyte interphase (SEI) formation, and can be ascribed to the occurrence of an irreversible conversion reaction in SnO_2 ($SnO_2 + 4Li^+ + 4e^- \rightarrow Sn + 2Li_2O$), which corresponds to a theoretical capacity of about 711 mAh g^{-1}.[22,25,38]

The untreated SnO_2 (B-SnO_2) electrode shows a low specific capacity of about 700 mAh g^{-1} at the 100th cycle, which is 50% lower than that of the post-deposition heat-treated SnO_2 electrode (A-SnO_2) at the same cycle. However, after exhibiting some sort of stability in the ~35–100 cycle window, B-SnO_2 reveals a sharp fall in specific capacity with increasing electrochemical cycle number, which leads to ~216 mAh g^{-1} capacity at the 500th cycle, which was even lower, and only 18% of the capacity of A-SnO_2 at the same cycle, as displayed in Fig. 2(c). The observed capacity of about 700 mAh g^{-1} up to the 100th cycle for B-SnO_2 was consistent with the reported experimental results for other SnO_2-based electrodes in the literature,[25,27,38] and can be attributed to the contribution from the reversible alloying/dealloying reaction ($Sn + xLi^+ + xe^- \leftrightarrow Li_xSn$) of SnO_2.[22,25,38] Here, the 'x' in the alloying/dealloying reaction signifies the number of Li atoms contained in the Li–Sn alloy, per metal (here Sn) atom. The ratio of the number of Li atoms to the number of metal atoms must be as high as possible to enhance the capacity of the working electrode.[38] Theoretically, for x = 4.4, maximum-Sn-lithiated-phase $Li_{22}Sn_5$ is obtained, which corresponds to a specific capacity of 783 mAh g^{-1}.

At 500 cycles, the capacity retention for B-SnO_2 is around 22% (and 29%) with respect to its initial 10th cycle (and 35th cycle), as displayed in Fig. 2(d). Such a phenomenon can be ascribed to the commonly observed pulverization issues associated with SnO_2-based electrodes,[39] leading to a sharp loss in capacity, compromising the stability of the electrode, and thus the performance of the overall battery. The low conductivity of SnO_2 is also one reason for the pulverization problem. The observed electrochemical performance of B-SnO_2 is consistent with reported literature involving SnO_2-film-based electrodes.[25,39,40] In this regard, it should be noted that most published reports with general SnO_2-based electrodes in LIB, presented a specific capacity only up to 100–200 cycles.[3,25,39,40]

Such large capacity fading after ~100 cycles was mostly overcome in the post-deposition treated SnO_2 electrode (A-SnO_2), as shown in Fig. 2(a), (b), and (d). A higher capacity retention of 56% (and 71%), with respect to its initial 10th cycle (and 35th cycle), was evident for A-SnO_2, as shown in Fig. 2(d), implying better conductivity, a lower Sn-coarsening effect in the system and a reduction in pulverization.

The rate performance of A-SnO_2 at current densities from 0.3 A g^{-1} (0.2C) to 3 A g^{-1} (2C) was studied, as shown in Fig. 3. Even at the high current densities (high rates) of 0.9 A g^{-1} (0.6C), 1.5 A g^{-1} (1C) and 3 A g^{-1} (2C), competitive discharge capacities of A-SnO_2 of ~1340 mAh g^{-1}, ~1100 mAh g^{-1} and ~800 mAh g^{-1} at 50, 60 and 110 cycles were maintained, respectively (blue open-circle plot, Fig. 3). Moreover, reversible capacities of ~1150 mAh g^{-1} and ~1350 mAh g^{-1} could be recovered after 120 and 150 cycles upon reducing the current to 0.9 A g^{-1} (0.6C) and 0.3 A g^{-1} (0.2C). For reference, the A-SnO_2 specific capacity at a constant current density, 0.3 A g^{-1} (0.2C), is presented (red solid-circle plot) along with that of the varying current density plot (blue open-circles), in Fig. 3. The results manifest the remarkable rate performance of the A-SnO_2 electrode, signifying preserved specific capacity even after repeated cycles at relatively high rates.

The explanation for such superior performance of A-SnO_2 has been explored through a study of cyclic voltametric

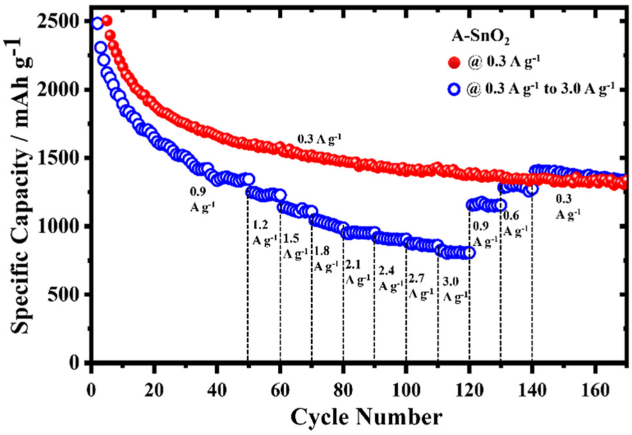

Fig. 3 Rate performance of A-SnO_2 at different current densities (rates) from 0.3 A g^{-1} (0.2C) to 3 A g^{-1} (2C).

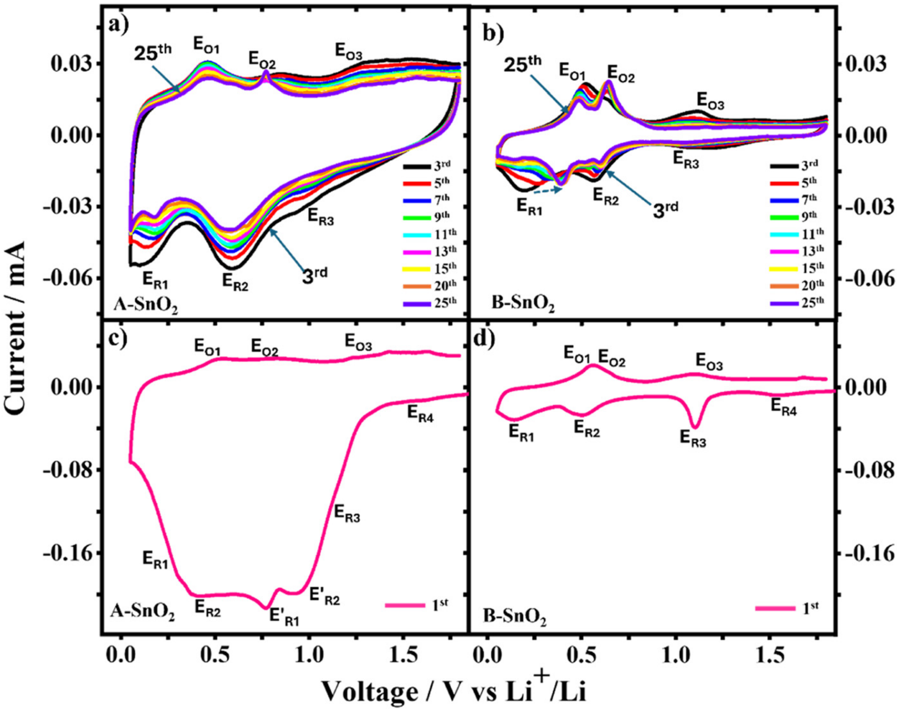

Fig. 4 Cyclic voltammogram (CV) of electrodes (a) A-SnO$_2$ and (b) B-SnO$_2$, for the 3rd, 5th, 7th, 9th, 11th, 13th, 15th, 20th, and 25th cycles at a scan rate of 0.05 mV s^{-1}. CV of the electrodes, (c) A-SnO$_2$ and (d) B-SnO$_2$, for the 1st cycle at the same scan rate of 0.05 mV s^{-1}.

response (CV), electrochemical impedance spectroscopy (EIS), FESEM and UV-vis spectroscopy.

Cyclic voltametric response (CV)

A typical CV scan of an A-SnO$_2$ electrode (with LiPF$_6$ electrolyte and metallic lithium as counter electrode, a similar assembly to that in GCD measurement) in the voltage window 0.05 to 1.8 V, focusing on the potential region of the lithium alloying–dealloying reaction,[41] at a slow scan rate of 0.05 mV s^{-1} is shown in Fig. 4(a). While the CV scan of B-SnO$_2$ with the same scan parameters is displayed in Fig. 4(b) for the purpose of comparison with same x–y scale. It can be seen that there are two pairs of redox peaks which appeared in the CV scan of A-SnO$_2$, corresponding to two predominant Li–Sn alloying and dealloying reactions, forming Li$_{22}$Sn$_5$ (0.18 V, 0.47 V) and LiSn (0.56 V, 0.76 V) phases,[41,42] depicted as (E_{R1}, E_{O1}) (E_{R2}, E_{O2}) in Fig. 4(a). When these results are compared with that of B-SnO$_2$, it can clearly be seen that the Li–Sn alloying reaction, E_{R1}, corresponding to Li$_{22}$Sn$_5$ (0.18 V), shifts rapidly towards a lower lithium-containing phase with increasing scan number, and saturates at about the Li$_7$Sn$_3$ (0.4 V) phase,[41,42] by 15 cycles, as depicted in Fig. 4(b). While the second redox reaction (E_{R2}, E_{O2}) corresponds to alloying with the lowest lithium-containing LiSn phase, exhibiting similar voltages to that of A-SnO$_2$.

Furthermore, Fig. 4 clearly shows the considerable enhancement in the area of the cyclic voltammogram of A-SnO$_2$ in comparison to B-SnO$_2$, implying the distinctively higher charge accumulation capacity or higher specific capacity[43] for the A-SnO$_2$ electrode, which is consistent with the GCD results, as discussed in the previous section. It is evident that the enhancement in the specific capacity relies predominantly on the emergence of significant capacitive behaviour in the A-SnO$_2$ electrode. To investigate the origin of such capacitive behaviour, the first cathodic scan (Fig. 4(c and d)) was carefully examined. In the first cathodic scan of B-SnO$_2$, there are a weak broad reduction band and an intense sharp band at 1.5 V and 1.1 V, respectively, which are ascribed to the two-step irreversible conversion reaction of SnO$_2$ ($SnO_2 + 4Li^+ + 4e^- \rightarrow Sn + 2Li_2O$),[22,28] denoted as E_{R4} and E_{R3}, respectively, in Fig. 4(d). However, in the first cathodic scan of A-SnO$_2$ (Fig. 3(c)), apart from a weak signal from E_{R4} at ~1.5 V, a broad intense reduction band appeared in the range of about 0.7–1.1 V. The broad intense band includes E_{R3}, and predominantly represents the intense two-step conversion reactions involving CuO to produce Cu and Li$_2$O ($CuO + 2Li^+ + 2e^- \leftrightarrow 2Cu_2O + Li_2O$; $Cu_2O + 2Li^+ + 2e^- \leftrightarrow 2Cu + Li_2O$) at 1.06 V ($E'_{R2}$) and 0.79 V ($E'_{R1}$), respectively,[44] which do not prevail in the reversed anodic scan (as the corresponding oxidation reactions from Cu to CuO take place above 2.4 V, which is beyond the set voltage window, 0.05–1.8 V, focused on the lithium alloying–dealloying reactions), and disappeared thereafter in the higher cycle cathodic scans. The formation of CuO in the A-SnO$_2$ system, and its reduction producing Li$_2$O after first discharge were also evident in the *ex situ* XPS results, as shown in SI, Fig. S1. While, the Cu current collector enables the formation of CuO, in consequence of the controlled post-deposition heat treatment of A-SnO$_2$. Essentially, such Cu/

Li_2O nanocomposites (or Me/Li_2O nanocomposites where Me represents transition metals that do not alloy with Li) are responsible for extra Li storage at low potential for rechargeable Li batteries,[45] and contributed interfacial charge storage resembling the characteristic of a capacitor, as established and reported in the literature.[45,46] The quantitative capacitive contribution[47] was estimated, which was found to be about 39%, as shown and described in SI, Fig. S2. In this regard, the differences in voltage profiles between samples A-SnO_2 and B-SnO_2 (Fig. 2(a) *vs.* 2(c)), as observed from the GCD study, signifying an additional capacitive contribution to the specific capacity of A-SnO_2 (Fig. 2(a)), obscuring the prominent plateaus as observed in B-SnO_2 (Fig. 2(c)) (*e.g.*, plateaus at 0.56 V and 0.47 V in the discharge and charge profiles, respectively) corresponding to Li alloying–dealloying reactions, further supports the above inference, revealing the extra Li storage through capacitive characteristics.

Hence, the origin of such observed higher stable capacity in the A-SnO_2 electrode relies on the formation of Cu/Li_2O nanocomposites, which plays the role of effectively enhancing the specific capacity through an interfacial charge storage mechanism *via* capacitive behaviour.[45] Surface morphology study and UV-vis results, as presented in the next sections, consistently support this inference.

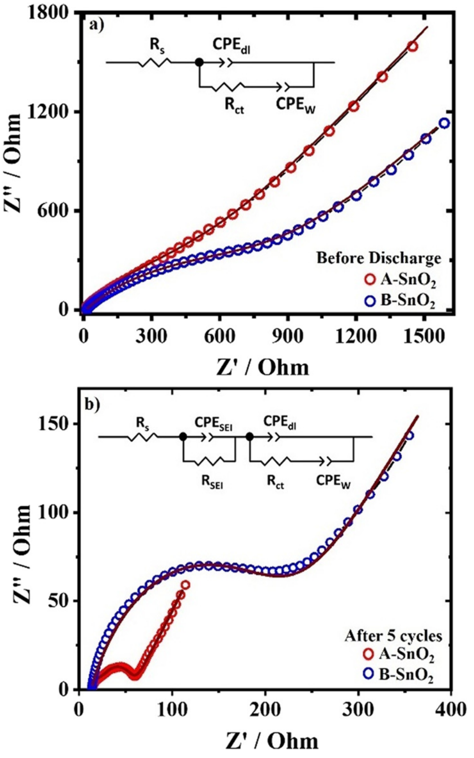

Fig. 5 Electrochemical impedance spectroscopy (EIS) data of A-SnO_2 (red open-circles) and B-SnO_2 (blue open-circles) electrodes before (a) and after (b) cycling, along with the corresponding fitting lines (solid-brown lines) using respective equivalent circuit models, as shown in the respective insets.

Overall, the results from CV are consistent with that of GCD. The CV results indicate that the peak voltages remain nearly constant, demonstrating electrochemical stability of the cathode after 15 cycles, which strongly supports the GCD results and the cycle performance data.

Electrochemical impedance spectroscopy (EIS)

Electrochemical impedance spectroscopy (EIS) spectra were recorded for cells with A-SnO_2 and B-SnO_2 electrodes, both after formation (Fig. 5(a)) and after cycling (Fig. 5(b)). The spectra were fitted using the equivalent circuit model (as shown in the insets),[48] which includes R_s, R_{ct}, CPE_{dl} and CPE_w. Here, R_s, R_{ct} and CPE_{dl} correspond to the solution resistance (from the electrolyte), the charge transfer resistance and constant phase elements representing double-layer capacitance, respectively.[48,49] The constant phase element, CPE_w, represents the Li-ion diffusion-related behaviour of the cell, which combines Li diffusion processes occurring at the electrode.[48–50] CPE_{SEI} and R_{SEI} (in Fig. 5(b)) represent the constant phase element related to non-ideal capacitance of the SEI layer and resistance for Li-ion diffusion in the SEI layer, respectively, which emerge during cycling.[49,51] Fig. 5 shows that the charge transfer resistance (R_{ct}) of a cell with the A-SnO_2 electrode is less than that of B-SnO_2, where the difference became more prominent after a few cycles of the cells, as evident in Fig. 5(a) and (b). As per the general convention, charge transfer resistance (R_{ct}) was estimated, by considering the EIS plot of the cycled electrode (for a few cycles),[49,52] which corresponds to Fig. 5(b). After cycling the batteries for a few cycles (5 cycles), the R_{ct} values for A-SnO_2 and B-SnO_2 were found to be about ~34 Ω and ~212 Ω, respectively (Fig. 5(b)). The results (Fig. 5(b)) indicate about 84% reduction in charge transfer resistance in the case of the A-SnO_2 system, the electrode of interest, in comparison to B-SnO_2, the untreated one. EIS data collected prior to battery cycling show R_{ct} values of about 980 Ω and 1093 Ω, respectively, for A-SnO_2 and B-SnO_2 (Fig. 5(a)). These

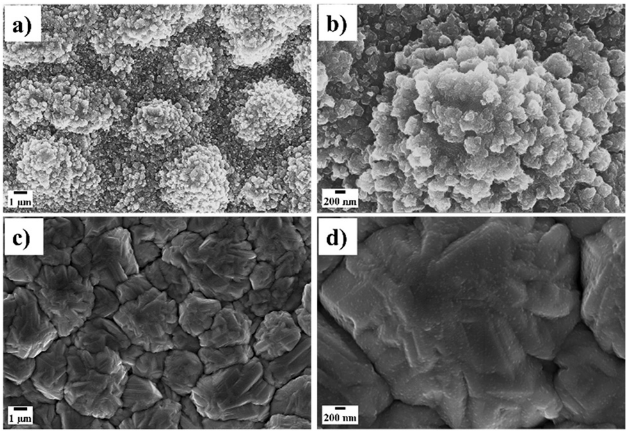

Fig. 6 FESEM images of A-SnO_2 ((a) and (b)) and B-SnO_2 ((c) and (d)) electrodes at two different magnifications along with respective scale bars.

findings indicate much less resistive interfaces formed by the A-SnO_2 over B-SnO_2, thereby contributing to the improved electrochemical performance, which supports the observed superior cycle performance from GCD profiles.

Morphology

Morphological information about the developed binder-free thin-film SnO_2-based electrodes was obtained by field emission scanning electron microscopy (FESEM), as displayed in Fig. 6.

Fig. 6(a and b) show FESEM images of the post-deposition heat-treated, binder-free A-SnO_2 electrode at two different magnifications. The images reveal a nanostructured flower with a nano-petal-like morphology, covering the entire electrode, which results in a large surface area and provides a suitable channel for ion transport, thereby improving charge transfer capability.[53] Moreover, the abundance of nanocrystallites in the electrode morphology helps to effectively reduce the induced volume stress, minimizing the pulverization problem.[30] Fig. 6(c and d) display the FESEM images of the corresponding untreated electrode, B-SnO_2, with equivalent magnification, for comparison purposes. It is evident that the A-SnO_2 electrode, possessing regularly arranged nanostructured subunits with numerous nano-voids and high specific area of void borders that facilitate the lithiation/de-lithiation process, shorten the Li^+ transfer distances and hinder Sn coarsening, resulting in an enhancement in lithium storage, and reaction reversibility. Furthermore, the larger electrochemical surface area (ECSA)[54] of A-SnO_2 compared to B-SnO_2 was also verified quantitively through EIS study, as described in SI, S2. Thus, this improved morphology facilitating smooth ion transportation within the A-SnO_2 electrode, also significantly contributed to the remarkable rate performance of the system, as evident in Fig. 3.

The results signify that the constituents, structure, conformation and advantageous morphology of A-SnO_2 provide a pathway for high interfacial charge storage capacity along with a higher amount of Li intercalation in the system, which efficiently activated the overall system, showing an improved electrochemical performance.

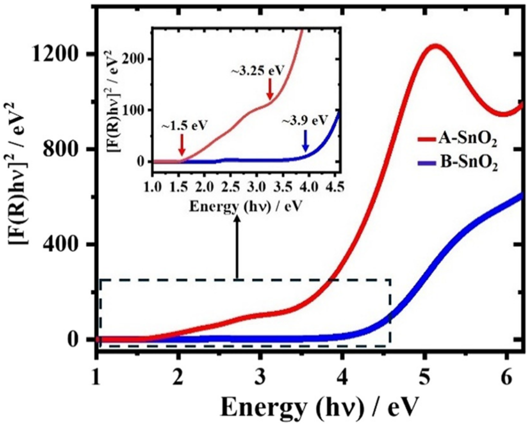

Fig. 7 UV-vis spectroscopy in diffuse reflectance (DRS) mode for A-SnO_2 (red line) and B-SnO_2 (blue line) electrodes. The zoomed portion of the data shown in the inset, indicates the effective band-edges of A-SnO_2 and B-SnO_2.

UV-vis study

The electronic properties, specifically the effective band edge or band gap, of the A-SnO_2 system was examined in comparison to B-SnO_2 *via* UV-vis spectroscopy in diffuse reflectance mode (DRS), as displayed in Fig. 7. The plot of $(F(R)h\nu)^2$ *versus* photon energy $h\nu$ is shown in Fig. 7, where $F(R)$ is the Kubelka–Munk function,[55] as represented in eqn (1), and R is the diffuse reflectance. The extrapolated line at $(F(R)h\nu)^2 = 0$ gives a tentative value for the band gap in eV.[56] $F(R)$ is proportional to the absorption coefficient, and can be expressed as[57]

$$F(R) = \frac{(1-R)^2}{2R} \tag{1}$$

The distinctive reduced effective absorption band-edge of the A-SnO_2 system (~3.25 eV and ~1.5 eV) compared to untreated B-SnO_2 (~4 eV) is evident in Fig. 7. The optical band-edge of B-SnO_2 is consistent with nanostructured SnO_2 systems.[58] However, the UV-vis plot of the A-SnO_2 electrode with a lower band-edge at 3.25 eV and below, indicates the incorporation of CuO nanostructures[59] into the SnO_2 system. The findings emphasize the interface-induced effect in the A-SnO_2 system, as a result of controlled growth and designed post-deposition treatment of the thin-film SnO_2 on the Cu current collector. Consistent results were obtained from attenuated total reflectance–Fourier transform infrared spectroscopy (ATR-FTIR), as demonstrated in SI, Fig. S3.

The results signify the controlled heat-treatment-induced interfacial phenomena at the SnO_2/Cu interface associated with the formation and dispersion/incorporation of CuO nanostructures into the SnO_2 nanocrystallite system. These results align with the inference obtained from the CV study; see Fig. 4 in the earlier section.

Hence, the overall studies signify that the observed superior performance of the post-deposition heat-treated SnO_2 electrode (A-SnO_2) in LIB relies on the formation of well-defined SnO_2 nanocrystallites along with the improved hierarchical surface morphology (see the FESEM images in Fig. 6) coupled with the interfacial phenomena. Such a novel architecture for the electrode results in significant enhancement in the effective conductivity of the system, improved charge transfer properties, prevention of pulverization, hindrance to Sn agglomeration, and, importantly, contributes to an extra interfacial Li storage capacity to the system with the aid of Cu/Li_2O nanocomposite formation (as detailed in the earlier section).

Experimental

Preparation of binder-free SnO_2-based electrodes

To prepare binder-free electrodes involving SnO_2 thin-film on Cu, the RF-magnetron sputtering deposition technique was used to deposit SnO_2 on Cu sheets. The thin Cu sheet (9 μm thick, MTI Corporation) acts as a current collector and substrate for SnO_2 sputter deposition. The SnO_2 target (two-inch diameter, 99.99% purity, Testbourne Ltd. UK) was used for sputtering purposes, under Ar gas (purity 99.999%) with a constant flow of 40 sccm, and sputtering power of 50 W. The distance between the target surface and the Cu foil was 14.1 cm. Base pressure and working pressure were maintained at $\sim 2.5 \times 10^{-5}$ bar and $\sim 1.9 \times 10^{-3}$ bar, respectively. The substrate holder was rotating at 30 rpm, and no heating was applied to the substrate holder during the deposition process. The thickness of SnO_2 was controlled by deposition time. The electrode mass was measured using an electronic balance (Sartorius SECURA225D-10IN weighing balance with an accuracy of 0.01 mg) before and after SnO_2 loading on the Cu current collector to calculate the mass of deposited SnO_2. In this method, the total mass of the deposited SnO_2 electrode material on a piece of Cu foil or current collector (of size 7.8 cm × 2.8 cm) was measured first, and was found to be 0.9 mg. The active electrode mass was then estimated to be 0.07 mg, based on the size or area of the circular electrode of diameter 15 mm, as used in the CR2032 coin cell. The estimated mass of the deposited SnO_2 binder-free electrode was also cross-verified through estimation of the SnO_2 film thickness *via* the cross-sectional FESEM image, as displayed in Fig. 1(b). The thickness of the deposited SnO_2 film was estimated from cross-sectional FESEM (Fig. 1(b)) as about 60 nm, considering the mass density of SnO_2 to be 6.9 gm cm^{-3} and the electrode mass appears to be 0.07 mg (for a 15 mm diameter electrode), which signifies consistency in the measurements and thus in the results.

After deposition, the SnO_2/Cu electrode was heat-treated in a muffle furnace at a temperature of 400 °C for a short time (about 10 minutes) in an air atmosphere at ambient pressure. Before and after post-deposition heat-treated SnO_2 thin film (of about 60 nm thickness, with an active mass loading of 0.07 mg or with a mass density of 0.04 mg cm^{-2}) on Cu current collector systems were referred to as untreated SnO_2 electrode "B-SnO_2" and electrode of interest "A-SnO_2", respectively. Photographs of A-SnO_2, B-SnO_2 and the bare Cu current collector are shown in SI, Fig. S4.

Assembling of coin cell and electrochemical measurements

The electrochemical performances of the A-SnO_2 and B-SnO_2 working electrodes were investigated with CR2032 coin cells assembled in an argon-filled glovebox (MBRAUN UNIlab Plus, Germany) in half-cell configuration with an Li chip (diameter 15 mm) as the counter electrode. A tri-layer polypropylene–polyethylene–polypropylene (PP/PE/PP) membrane (Celgard 2325) was used as a separator (diameter 20 mm). An electrolyte solution of 1 M $LiPF_6$ salt (Sigma Aldrich) was prepared with a mixture of dimethyl carbonate (DMC) and ethylene carbonate (EC) in a 1 : 1 volume ratio. Cyclic performance and galvanostatic charge/discharge (GCD) cycling tests were conducted using a battery testing system (NEWARE BTS4000), and electrochemical workstations (CH instruments, CHI423B and CHI605E) at a current density of 0.3 A g^{-1}, over a voltage range of 0.02 V to 1.8 V, at room temperature. The specific charge and discharge capacities of the electrodes were determined by dividing the total electrode capacity by the electrode mass (mass of the SnO_2). Cyclic voltammetry (CV) was conducted using electrochemical workstations (CHI605E) within a voltage range of 0.05 V to 1.8 V at a scan speed of 0.05 mV s^{-1}. Electrochemical impedance spectroscopy (EIS) measurements were conducted using an electrochemical workstation (CHI423B), applying a sine wave with an amplitude of 5.0 mV over frequencies from 10^5 Hz to 0.05 Hz.

Characterization techniques

Morphological studies were conducted using a field emission scanning electron microscope (FE-SEM Supra 55, Carl Zeiss, Germany). Cross-sectional FESEM images were taken using an FEI Nova Nano SEM 450 field emission scanning electron microscope. Optical characterization was carried out using the diffused reflectance spectroscopy (DRS) mode of a UV-visible spectrophotometer (Shimadzu UV-2600i) equipped with an integrating sphere, in the wavelength range 200 nm to 1400 nm. The structural analysis of A-SnO_2 and B-SnO_2 samples was conducted using the X-ray diffraction (XRD) technique using a Rigaku SmartLab, Japan with a Cu Kα X-ray source (40 kV, 1.2 kW). The XRD data were recorded at a scan rate of 0.1° min^{-1} at a 2θ range of 20–60° with a step size of 0.01°. Vibrational studies were conducted using ATR FTIR spectroscopy (L1600300 Spectrum TWO FTIR spectrometer, Perkin Elmer), at a wavenumber range 900 cm^{-1} to 400 cm^{-1}. X-ray photoelectron spectroscopy (XPS) was recorded using a SPECS Surface Nano Analysis GmbH, Germany, in the binding energy range of 1300 eV to 0 eV, using an Al Kα (1486.1 eV) X-ray source (13 kV, 100 W). XPS study of the pristine SnO_2 electrode (B-SnO_2) (as shown in Fig. 1(a)) was conducted using the AIPES beamline (BL-02) of Indus-1 synchrotron source, RRCAT, Indore, India, with an Omicron energy analyzer (EA-125, Germany). All core-level spectra were calibrated using the C 1s (284.6 eV) peak.

Conclusions

We demonstrate the interface-induced significant stability, cycle life, and overall high capacity of the tin-oxide (SnO_2)-based thin-film electrode with a Cu current collector in a rechargeable Li-ion battery (LIB). Post-deposition, controlled heat treatment of optimized SnO_2 thin film on a Cu current collector allows the augmented growth of structured interfaces and overall hierarchical nanostructured morphology, which provides adequate electrical connectivity in the electrode system, making the system better conducting and more resilient towards electrochemical cycling, suppressing pulverization issues, and exhibiting high stability and long cycle life. Moreover, the beneficial structured interface not only provides good electrical connectivity but also allows the growth of Cu/Li_2O nanocomposites from the initial battery cycling process, which contributes to extra Li storage and enhances capacity effectively through an interfacial charge storage mechanism *via* capacitive characteristics. Essentially, the electrode yields a superior specific capacity, additionally deploying interfacial charge storage.

Quantitatively, the prototype of rechargeable LIB developed in this work consists of a lightweight, binder-free, cost-effective, environmentally friendly SnO_2-based electrode on a Cu current collector (A-SnO_2), with Li as the counter electrode. This configuration delivers high reversible capacity, stability and remarkable cycle life (1430 mAh g^{-1} and about 1200 mAh g^{-1} after 100 and 500 cycles, respectively, at a current density of 0.3 A g^{-1} (0.2C)). This electrode also exhibits excellent rate-performance (800 mAh g^{-1} at 3 A g^{-1} (2C) at 110 cycles), with high Coulombic efficiency (98–99%). In comparison, a conventional SnO_2 thin-film anode shows much lower reversible capacities of about 700 mAh g^{-1} and 216 mAh g^{-1}, at the 100th cycle and 500th cycles, respectively, under the same current density of 0.3 A g^{-1} (as demonstrated here for B-SnO_2, and other reported results in the literature based on SnO_2 thin-film electrodes).

This electrode demonstrated a higher level of performance than thin-film anodes used in equivalent micro-battery systems reported in the literature (Table S1). These findings highlight the potential of SnO_2-based electrodes with interfacial engineering to satisfy the requirements for cost-effective, lightweight microelectronic energy storage devices, while also guiding the design of advanced materials for next-generation energy storage systems.

Author contributions

Adi Pratap Singh and Banadeep Dutta: co-first authors, equal contribution, methodology, formal analysis, data curation, validation, investigation, visualization, writing – original draft. Sudeshna Chattopadhyay: corresponding author, conceptualization, funding acquisition, resources, methodology, project administration, writing – review & editing, visualization, validation, supervision.

Conflicts of interest

There are no conflicts to declare.

Data availability

The authors confirm that the data supporting the findings of this study are available within the article and in its supplementary information (SI).

Supplementary information: XPS and XRD results of A-SnO_2 electrode before and after 1st discharge, attenuated total reflectance-Fourier transform infrared spectroscopy (ATR-FTIR) results, comparison table for battery performance with A-SnO_2 and other thin-film electrodes, quantification of the electrochemically active surface area (ECSA) of A-SnO_2 and B-SnO_2 electrodes from EIS data, quantitative estimation of capacitive contribution to Li-ion charge storage for A-SnO_2 electrode, photographs of A-SnO_2 and B-SnO_2 electrodes. See DOI: **https://doi.org/10.1039/d5lf00261c**.

Acknowledgements

We would acknowledge Indian Institute of Technology Indore for all kinds of support for this work. We would acknowledge the Science and Engineering Research Board (SERB), India, Project No. CRG/2020/005595 for supporting this work. We would like to thank Dr. Uday Deshpande and Sachin Kumar (UGC-DAE CSR, Indore) for XPS measurements and Dr. Gunjan Verma (UGC-DAE CSR, Indore) for cross-sectional SEM measurements. We would also like to thank Dr. R. J. Choudhary and Mr. Sharad Karwal (UGC-DAE CSR, Indore) for XPS measurements at the Indus-1 synchrotron radiation source, RRCAT, Indore, India. A. P. S. is thankful to CSIR-UGC INDIA, New Delhi under the UGC-Ref. No. 221610040822, and B. D. is thankful to DST INSPIRE-INDIA, New Delhi under the Award No. IF210393 for providing the fellowships.

Notes and references

1 G. De Carne, S. M. Maroufi, H. Beiranvand, V. De Angelis, S. D'Arco, V. Gevorgian, S. Waczowicz, B. Mather, M. Liserre and V. Hagenmeyer, *Electr. Power Syst. Res.*, 2024, **236**, 110963.
2 F. Mwasilu, J. J. Justo, E.-K. Kim, T. D. Do and J.-W. Jung, *Renewable Sustainable Energy Rev.*, 2014, **34**, 501–516.
3 S. Zhao, C. D. Sewell, R. Liu, S. Jia, Z. Wang, Y. He, K. Yuan, H. Jin, S. Wang, X. Liu and Z. Lin, *Adv. Energy Mater.*, 2020, **10**, 1902657.
4 P. Poizot, S. Laruelle, S. Grugeon, L. Dupont and J. M. Tarascon, *Nature*, 2000, **407**, 496–499.
5 J. B. Goodenough and K.-S. Park, *J. Am. Chem. Soc.*, 2013, **135**, 1167–1176.
6 H. B. Wu, J. S. Chen, H. H. Hng and X. Wen Lou, *Nanoscale*, 2012, **4**, 2526–2542.
7 (*a*) M. Armand and J. M. Tarascon, *Nature*, 2008, **451**, 652–657; (*b*) C.-X. Zu and H. Li, *Energy Environ. Sci.*, 2011, **4**, 2614–2624.
8 (*a*) H. Wang, Y. Bai, S. Chen, X. Luo, C. Wu, F. Wu, J. Lu and K. Amine, *ACS Appl. Mater. Interfaces*, 2015, **7**, 80–84; (*b*) D. Pal, A. Mathur, A. Singh, S. Pakhira, R. Singh and S. Chattopadhyay, *ChemistrySelect*, 2018, **3**, 12512–12523.
9 Y. Kang, C. Deng, Y. Chen, X. Liu, Z. Liang, T. Li, Q. Hu and Y. Zhao, *Nanoscale Res. Lett.*, 2020, **15**, 112.
10 K. Sun, T.-S. Wei, B. Y. Ahn, J. Y. Seo, S. J. Dillon and J. A. Lewis, *Adv. Mater.*, 2013, **25**, 4539–4543.
11 H. Liu, G. Zhang, X. Zheng, F. Chen and H. Duan, *Int. J. Extreme Manuf.*, 2020, **2**, 042001.

12 L. Zhang, X. Liu, M. Zhong, Y. Zhou, Y. Wang, T. Yu, X. Xu, W. Shen, L. Yang, N. Liu, D. Wei and Z. Liu, *Appl. Mater. Today*, 2020, **20**, 100651.

13 P. G. de Gennes, *Rev. Mod. Phys.*, 1985, **57**, 827–863.

14 (*a*) L. Bricotte, K. Chougrani, V. Alard, V. Ladmiral and S. Caillol, *Int. J. Adhes. Adhes.*, 2024, **132**, 103673; (*b*) S. Kisin, P. G. T. van der Varst and G. de With, *Thin Solid Films*, 2007, **515**, 6853–6859.

15 E. M. Petrie, in *Joining Textiles*, ed. I. Jones and G. K. Stylios, Woodhead Publishing, 2013, pp. 225–274.

16 (*a*) L. I. Maissel, R. Glang and P. P. Budenstein, *J. Electrochem. Soc.*, 1971, **118**, 114C; (*b*) R. J. MacDonald and D. Haneman, *J. Appl. Phys.*, 1966, **37**, 3048–3056.

17 W.-J. Li, W.-Z. Shao, Q. Chen, L. Zhang, Y. Han, B.-A. Chen, Q. Wang and L. Zhen, *Phys. Chem. Chem. Phys.*, 2018, **20**, 15618–15625.

18 M. N. Obrovac and V. L. Chevrier, *Chem. Rev.*, 2014, **114**, 11444–11502.

19 (*a*) J. Cabana, L. Monconduit, D. Larcher and M. R. Palacín, *Adv. Mater.*, 2010, **22**, E170–E192; (*b*) T. Li, X. Li, Z. Wang, H. Guo and Y. Li, *J. Mater. Chem. A*, 2015, **3**, 11970–11975; (*c*) J. Leng, Z. Wang, X. Li, H. Guo, H. Li, K. Shih, G. Yan and J. Wang, *J. Mater. Chem. A*, 2017, **5**, 14996–15001; (*d*) T. Li, X. Li, Z. Wang, H. Guo, Y. Li and J. Wang, *J. Mater. Chem. A*, 2017, **5**, 13469–13474.

20 (*a*) J. Read, D. Foster, J. Wolfenstine and W. Behl, *J. Power Sources*, 2001, **96**, 277–281; (*b*) Y. Idota, T. Kubota, A. Matsufuji, Y. Maekawa and T. Miyasaka, *Science*, 1997, **276**, 1395–1397; (*c*) P. Meduri, C. Pendyala, V. Kumar, G. U. Sumanasekera and M. K. Sunkara, *Nano Lett.*, 2009, **9**, 612–616; (*d*) Y. Wang, H. C. Zeng and J. Y. Lee, *Adv. Mater.*, 2006, **18**, 645–649; (*e*) J. S. Chen and X. W. Lou, *Small*, 2013, **9**, 1877–1893.

21 (*a*) R. Retoux, T. Brousse and D. M. Schleich, *J. Electrochem. Soc.*, 1999, **146**, 2472; (*b*) K. D. Kepler, J. T. Vaughey and M. M. Thackeray, *J. Power Sources*, 1999, **81-82**, 383–387.

22 R. Hu, D. Chen, G. Waller, Y. Ouyang, Y. Chen, B. Zhao, B. Rainwater, C. Yang, M. Zhu and M. Liu, *Energy Environ. Sci.*, 2016, **9**, 595–603.

23 Y.-H. Jin, K.-M. Min, S.-D. Seo, H.-W. Shim and D.-W. Kim, *J. Phys. Chem. C*, 2011, **115**, 22062–22067.

24 (*a*) B. Jiang, Y. He, B. Li, S. Zhao, S. Wang, Y.-B. He and Z. Lin, *Angew. Chem., Int. Ed.*, 2017, **56**, 1869–1872; (*b*) J. Ren, J. Yang, A. Abouimrane, D. Wang and K. Amine, *J. Power Sources*, 2011, **196**, 8701–8705; (*c*) S. D. Ponja, B. A. D. Williamson, S. Sathasivam, D. O. Scanlon, I. P. Parkin and C. J. Carmalt, *J. Mater. Chem. C*, 2018, **6**, 7257–7266.

25 R. Hu, H. Zhang, Z. Lu, J. Liu, M. Zeng, L. Yang, B. Yuan and M. Zhu, *Nano Energy*, 2018, **45**, 255–265.

26 R. Hu, G. H. Waller, Y. Wang, Y. Chen, C. Yang, W. Zhou, M. Zhu and M. Liu, *Nano Energy*, 2015, **18**, 232–244.

27 V. Aravindan, K. B. Jinesh, R. R. Prabhakar, V. S. Kale and S. Madhavi, *Nano Energy*, 2013, **2**, 720–725.

28 (*a*) L. Zu, Q. Su, F. Zhu, B. Chen, H. Lu, C. Peng, T. He, G. Du, P. He, K. Chen, S. Yang, J. Yang and H. Peng, *Adv. Mater.*, 2017, **29**, 1701494; (*b*) J. Liang, X.-Y. Yu, H. Zhou, H. B. Wu, S. Ding and X. W. Lou, *Angew. Chem., Int. Ed.*, 2014, **53**, 12803–12807.

29 C. Xu, J. Sun and L. Gao, *J. Mater. Chem.*, 2012, **22**, 975–979.

30 A. A. AbdelHamid, A. Mendoza-Garcia and J. Y. Ying, *Nano Energy*, 2022, **93**, 106860.

31 (*a*) L. Yu, X. Zhou, L. Lu, X. Wu and F. Wang, *ChemSusChem*, 2020, **13**, 5361–5407; (*b*) E. Poorshakoor and M. Darab, *J. Energy Storage*, 2024, **75**, 109638.

32 B. Huang, J. Yang, Y. Zou, L. Ma and X. Zhou, *Electrochim. Acta*, 2014, **143**, 63–69.

33 (*a*) A. Sedky, N. Afify, A. Hakamy and A. M. Abd-Elnaiem, *Phys. Scr.*, 2023, **98**, 125929; (*b*) A. Peter, P. de Julio and K. James, *Atkins' Physical Chemistry*, 2022; (*c*) G. E. Adesakin, O. G. Edema, A. O. Akinbolusere and G. O. Okocha, *NIPES - Journal of Science and Technology Research*, 2023, **5**, 264–271.

34 (*a*) M. Batzill, J. Kim, D. E. Beck and B. E. Koel, *Phys. Rev. B: Condens. Matter Mater. Phys.*, 2004, **69**, 165403; (*b*) X. Liu, Y. Jiang, K. Li, F. Xu, P. Zhang and Y. Ding, *Mater. Res. Bull.*, 2019, **109**, 41–48; (*c*) W. Li, C. Shen, G. Wu, Y. Ma, Z. Gao, X. Xia and G. Du, *J. Phys. Chem. C*, 2011, **115**, 21258–21263; (*d*) F. A. Akgul, C. Gumus, A. O. Er, A. H. Farha, G. Akgul, Y. Ufuktepe and Z. Liu, *J. Alloys Compd.*, 2013, **579**, 50–56.

35 A. R. Selvaraj, M. Hong, H. Koo, J. Mun and H.-K. Kim, *J. Power Sources*, 2024, **591**, 233821.

36 (*a*) T. Brousse, R. Retoux, U. Herterich and D. M. Schleich, *J. Electrochem. Soc.*, 1998, **145**, 1; (*b*) J. P. Maranchi, A. F. Hepp and P. N. Kumta, *Electrochem. Solid-State Lett.*, 2003, **6**, A198; (*c*) R. Lin, S. Zhang, Z. Du, H. Fang, Y. Ren and X. Wu, *RSC Adv.*, 2015, **5**, 87090–87097; (*d*) A. A. Arie and J. K. Lee, *Mater. Sci. Forum*, 2013, **737**, 80–84; (*e*) Y. Xia, B. Sun, S. Zhu, S. Mao, X. Li, B. Guo, Y. Zeng, H. Wang and Y. Zhao, *J. Solid State Chem.*, 2019, **269**, 132–137; (*f*) W. Chen, H. Zhang, B. Yang, B. Li and Z. Li, *Thin Solid Films*, 2019, **672**, 157–164; (*g*) F. Klein, R. Pinedo, P. Hering, A. Polity, J. Janek and P. Adelhelm, *J. Phys. Chem. C*, 2016, **120**, 1400–1414; (*h*) L. Cao, D. Wang and R. Wang, *Mater. Lett.*, 2014, **132**, 357–360; (*i*) G. Evmenenko, T. T. Fister, D. B. Buchholz, Q. Li, K.-S. Chen, J. Wu, V. P. Dravid, M. C. Hersam, P. Fenter and M. J. Bedzyk, *ACS Appl. Mater. Interfaces*, 2016, **8**, 19979–19986; (*j*) Y. Wang, Y.-F. Zhang, H.-R. Liu, S.-J. Yu and Q.-Z. Qin, *Electrochim. Acta*, 2003, **48**, 4253–4259; (*k*) N. Garino, A. Lamberti, R. Gazia, A. Chiodoni and C. Gerbaldi, *J. Alloys Compd.*, 2014, **615**, S454–S458; (*l*) S. K. Sharma, M.-S. Kim, D. Y. Kim and J.-S. Yu, *Electrochim. Acta*, 2013, **87**, 872–879; (*m*) X. Teng, Y. Qin, X. Wang, H. Li, X. Shang, S. Fan, Q. Li, J. Xu, D. Cao and S. Li, *Nanoscale Res. Lett.*, 2018, **13**, 60.

37 (*a*) J. S. Kim, S. S. Kim, S. J. Kim, S. M. Lee, K. Y. Sheem and G. J. Jeong, US20050164090, Samsung SDI Co Ltd, 2005; (*b*) L. A. Archer, US20110300447, Cornell University, 2001.

38 T. Brousse, D. Defives, L. Pasquereau, S. M. Lee, U. Herterich and D. M. Schleich, *Ionics*, 1997, **3**, 332–337.

39 (*a*) Y. Lei, N. Du, W. Liu, H. Wu and D. Yang, *Ionics*, 2019, **25**, 4651–4658; (*b*) L. Yang, T. Dai, Y. Wang, D. Xie, R. L. Narayan, J. Li and X. Ning, *Nano Energy*, 2016, **30**, 885–891.

40 H. Wang, Q. Liang, W. Wang, Y. An, J. Li and L. Guo, *Cryst. Growth Des.*, 2011, **11**, 2942–2947.

41 Z. Chen, Y. Cao, J. Qian, X. Ai and H. Yang, *J. Mater. Chem.*, 2010, **20**, 7266–7271.

42 (*a*) C. Wang, A. John Appleby and F. E. Little, *J. Power Sources*, 2001, **93**, 174–185; (*b*) R. A. Guidotti and P. J. Masset, *J. Power Sources*, 2008, **183**, 388–398; (*c*) H. Mukaibo, T. Sumi, T. Yokoshima, T. Momma and T. Osaka, *Electrochem. Solid-State Lett.*, 2003, **6**, A218.

43 (*a*) L. E. Helseth, *J. Energy Storage*, 2021, **35**, 102304; (*b*) Y. Huang, M. Zhong, Y. Huang, M. Zhu, Z. Pei, Z. Wang, Q. Xue, X. Xie and C. Zhi, *Nat. Commun.*, 2015, **6**, 10310.

44 (*a*) A. Li, H. Song, W. Wan, J. Zhou and X. Chen, *Electrochim. Acta*, 2014, **132**, 42–48; (*b*) S. Q. Wang, J. Y. Zhang and C. H. Chen, *Scr. Mater.*, 2007, **57**, 337–340.

45 (*a*) Y. F. Zhukovskii, P. Balaya, E. A. Kotomin and J. Maier, *Phys. Rev. Lett.*, 2006, **96**, 058302; (*b*) J. Jamnik and J. Maier, *Phys. Chem. Chem. Phys.*, 2003, **5**, 5215–5220.

46 (*a*) B. Zhao, F. Mattelaer, J. Kint, A. Werbrouck, L. Henderick, M. Minjauw, J. Dendooven and C. Detavernier, *Electrochim. Acta*, 2019, **320**, 134604; (*b*) A. Sahai, N. Goswami, S. D. Kaushik and S. Tripathi, *Appl. Surf. Sci.*, 2016, **390**, 974–983.

47 (*a*) W. Liu, P. Xiang, X. Dong, H. Yin, H. Yu, P. Cheng, S. Zhang and S. Shi, *Composites, Part B*, 2021, **216**, 108883; (*b*) J. Xie, X. Li, H. Lai, Z. Zhao, J. Li, W. Zhang, W. Xie, Y. Liu and W. Mai, *Angew. Chem., Int. Ed.*, 2019, **58**, 14740–14747; (*c*) Z. Li, G. Li, W. Xu, M. Zhou, C. Xu, M. Shi, F. Li, L. Chen and B. He, *ChemElectroChem*, 2018, **5**, 2774–2780.

48 (*a*) J. Li, E. Murphy, J. Winnick and P. A. Kohl, *J. Power Sources*, 2001, **102**, 294–301; (*b*) M. E. Orazem and B. Ulgut, *J. Electrochem. Soc.*, 2024, **171**, 040526.

49 D. Guan, J. Li, X. Gao and C. Yuan, *J. Alloys Compd.*, 2014, **617**, 464–471.

50 D. Cavaliere, A. Ikezawa, T. Okajima and H. Arai, *J. Power Sources*, 2024, **621**, 235316.

51 S. A. Palaparty, R. L. Patel and X. Liang, *RSC Adv.*, 2016, **6**, 24340–24348.

52 L.-H. Wang, S. Gao, L.-L. Ren, E.-L. Zhou and Y.-F. Qin, *Front. Chem.*, 2021, **9**, 790659.

53 Y. Zhu, J. Li, M. S. Saleh, H. Pham, T. P. Plateau, R. Panat and J. Park, *J. Power Sources*, 2020, **476**, 228593.

54 (*a*) C. C. L. McCrory, S. Jung, I. M. Ferrer, S. M. Chatman, J. C. Peters and T. F. Jaramillo, *J. Am. Chem. Soc.*, 2015, **137**, 4347–4357; (*b*) C. C. L. McCrory, S. Jung, J. C. Peters and T. F. Jaramillo, *J. Am. Chem. Soc.*, 2013, **135**, 16977–16987; (*c*) B. Hirschorn, M. E. Orazem, B. Tribollet, V. Vivier, I. Frateur and M. Musiani, *Electrochim. Acta*, 2010, **55**, 6218–6227.

55 B. J. Wood and R. G. J. Strens, *Mineral. Mag.*, 1979, **43**, 509–518.

56 S. Landi, I. R. Segundo, E. Freitas, M. Vasilevskiy, J. Carneiro and C. J. Tavares, *Solid State Commun.*, 2022, **341**, 114573.

57 S. Aksoy, Y. Çağlar, M. Caglar and S. Ilican, *J. Nanoelectron. Optoelectron.*, 2016, **11**, 115–121.

58 (*a*) M. Mezyen, G. El Fidha, N. Bitri, F. Harrathi, I. Ly and E. Llobet, *RSC Adv.*, 2023, **13**, 31151–31166; (*b*) A. Ahmed, M. Naseem Siddique, U. Alam, T. Ali and P. Tripathi, *Appl. Surf. Sci.*, 2019, **463**, 976–985; (*c*) G. Pang, S. Chen, Y. Koltypin, A. Zaban, S. Feng and A. Gedanken, *Nano Lett.*, 2001, **1**, 723–726.

59 (*a*) P. Vinothkumar, C. Manoharan, B. Shanmugapriya and M. Bououdina, *J. Mater. Sci.: Mater. Electron.*, 2019, **30**, 6249–6262; (*b*) L. Xu, G. Zheng, S. Pei and J. Wang, *Optik*, 2018, **158**, 382–390; (*c*) Y. Wang, S. Lany, J. Ghanbaja, Y. Fagot-Revurat, Y. P. Chen, F. Soldera, D. Horwat, F. Mücklich and J. F. Pierson, *Phys. Rev. B*, 2016, **94**, 245418; (*d*) N. Serin, T. Serin, Ş. Horzum and Y. Çelik, *Semicond. Sci. Technol.*, 2005, **20**, 398.